Chemical mechanism of allosteric and asymmetric dark reversion in a bacterial phytochrome uncovered by cryo-EM.

Authors

Szabolcs Bódizs[1^], Anna-Lena M. Fischer[1^], Miklós Cervenak[1], Sayan Prodhan[1], Michal Maj[2], and Sebastian Westenhoff[1,*]

Affiliations

[1] Department of Chemistry - BMC, Biochemistry, Uppsala University, 75123 Uppsala, Sweden

[2]Department of Chemistry - Ångström, Uppsala University, 75123 Uppsala, Sweden

[^]Equal contribution

[*]Lead contact

[*]Correspondence to: sebastian.westenhoff@kemi.uu.se

Author contributions

S.W. and M.M. designed the project; S.B., A.F., and S.W. planned the project and the experiments; S.B. purified the protein; S.B. and M.C. produced the grids and performed the single-particle cryo-EM data acquisition and refinement. S.B. interpreted the structures together with S.W.; S.P. performed the spectroscopic model prediction; A.F. performed the molecular dynamics simulations; S.W. secured funding; S.W. supervised the project; S.B., A.F., M.C., and S.W. wrote the paper with input from all authors.

Competing interest statement

The authors declare no competing interests.

Classification

Biological Sciences - Biophysics and Computational Biology

Keywords

cryo-electron microscopy ● molecular dynamics ● *Pseudomonas aeruginosa* ● photoreceptor ● allostery

This PDF file includes:

Main Text
Figures 1-4
Table 1

Abstract

Phytochromes are light-sensitive proteins found in plants, fungi, and bacteria. They switch between two functional states, Pr and Pfr, distinguished by E/Z isomers of their bilin chromophore. The chromophore can photoswitch between these states, but also thermally react in darkness. Given the high activation energy of the isomerization reaction in solution, it remains unclear how this reaction can proceed in the dark within the phytochrome. Here, we present time-resolved single-particle cryo-EM structures of the *Pseudomonas aeruginosa* bacteriophytochrome (*Pa*BphP) captured at multiple time points during dark reversion from Pr to Pfr. We identify structural asymmetries in the precursor Pr state stretching from the homodimer interface to a conserved histidine (H277) next to the bilin and find that these lead to a strong imbalance of the dark reversion reaction rate of the two protomers. Supported by molecular modelling, we conclude that small, protomer-dependent changes of the conserved histidine control the hydrogen-bonding network around the chromophore, thereby exerting control over the activation energy of the isomerization reaction. This mechanism explains how phytochromes can thermally dark revert and how allosteric control is asserted; and it provides a structural framework for tuning phytochrome signaling lifetimes in optogenetic applications.

Significance statement

The dark reversion reaction of phytochromes is crucial for their signalling role in plants, bacteria, and fungi, but it is vastly understudied in terms of its chemical mechanism. It remains unsolved how the reaction can proceed at all, given that the activation energy is prohibitively high for the isomerization to occur in solution. Using state-of-the-art time-resolved cryo-EM, we present a pioneering chemical and structural framework for understanding how the protein binding pocket regulates the reaction. Additionally, our results provide a rare example of strongly asymmetric reactivity across a dimeric protein, and explain the widely observed allostery of the dark reversion reaction in phytochromes. This opens up for rational engineering of the lifetimes of the signalling states in phytochromes.

Main Text

Introduction

Phytochromes are universal and adaptable light sensors that regulate diverse biological processes across plants, bacteria, and fungi.[1–3] These versatile photoreceptor proteins enable organisms to perceive and respond to light, temperature, and other environmental cues, influencing a wide array of physiological functions.[4–6] In plants, phytochromes are central to developmental and stress response pathways, contributing significantly to fitness in natural environments and productivity in agriculture.[7–9] Their mechanisms of action are diverse, involving changes in subcellular localization, protein-protein interactions, and crosstalk with other photoreceptors.[9–12] In bacteria, they frequently act as histidine kinases in two-component signalling systems, although a variety of alternative output domains have evolved.[4,13]

Central to phytochrome function is their ability to reversibly switch between a red light-absorbing Pr state and a far-red light-absorbing Pfr state. This allows organisms to sense the ratio of red to far-red light in their environment. The photoswitching is initiated by light-driven Z/E isomerization of a covalently bound bilin chromophore within a conserved photosensory core module (PAS-GAF-PHY, see **Fig. 1b**).[14] Structural studies have revealed key conformational changes between Pr and Pfr, including isomerization of the chromophore, refolding of the "PHY-tongue" motif, and rearrangements of the quaternary structure.[15–20] NMR and spectroscopic studies have shown that the chromophore-binding pocket sustains multiple conformational states,[21] and, more recently, single-particle cryo-electron microscopy (cryo-EM) structures have started to provide insights into full-length phytochrome architecture in near-native conditions.[22–28]

In the absence of light, phytochromes return to their resting states. Most phytochromes dark-revert to the Pr state, although "bathy" bacterial phytochromes revert to Pfr.[29] The dark reversion rates are species-dependent and modulated by pH, phosphorylation, and protein-protein interactions.[30–33] Dark reversion plays a key functional role by determining the lifetime of the photoactivated state and thus tuning the organism's sensitivity to ambient light cues. Evolution of paralogous genes allows plants to host several isoforms of phytochromes with different dark reversion rates, which, despite having partially similar spectral properties, can cater for a large dynamic range of signalling.[34] Additionally, since the reversion rate is highly temperature-dependent, phytochromes can act as biological thermometers.[6,35,36] The examples show that the thermal reversion of phytochromes is a key property of phytochromes, and that the protein must be able to control the thermal reversion reaction in the bilin chromophore. However, the structural and chemical basis for this remains poorly understood.

Phytochromes are typically dimeric proteins. This significantly enhances the signaling capabilities of the proteins, exemplified by the formation of PrPfr heterodimers, creating a distinct "third state" in addition to the PrPr and PfrPfr homodimers.[5,25,37] In *Arabidopsis thaliana* PhyB the PrPfr heterodimer undergoes dark reversion approximately 100 times faster than the PfrPfr homodimer, which indicates strong intra-dimeric allostery and leads to effective suppression of PhyB-mediated signaling under low light intensity.[38] While the existence of heterodimeric states has long been recognized in plants, evidence for PrPfr states in bacterial phytochromes is scarce. To date, only one crystal structure of an engineered bacterial phytochrome and a recent cryo-EM structure from a myxobacterial phytochrome have captured such hybrid forms.[20,25] In our recent work using optical spectroscopy, we show that PrPfr

heterodimeric states are indeed populated during dark reversion in bacterial phytochromes.[39] Notably, even in this bacterial phytochrome, we observed clear evidence of allosteric regulation of the dark reversion rate.

Despite its physiological importance, dark reversion remains poorly understood at the structural and chemical level. For thermal reversion, the chromophore has to isomerize around the 15-16 double bond (**Fig. S1**), which is expected to have a substantial activation energy on the order of 100 kJ/mol.[40] This corresponds to about 40 times the kT at 298 K, and thus prohibitively slow rates are expected. However, faster rates are observed, implying that chemical mechanisms must be at play to lower the activation energy. One scheme that fulfils this requirement is the keto-enol tautomerization on the D-ring of the biliverdin in its Pr form, which reduces the bond order of the C15-C16 bond and hence lowers the activation barrier for thermal reversion.[41,42] Using pH-dependent spectroscopy, Escobar et al. suggested that the concentration of the reversion-ready enol state may be controlled by one of the histidines in the vicinity of the chromophore.[43] Moreover, the rates are highly species-dependent and mutations in the vicinity of the chromophore sensitively influence the dark reversion rates.[44] These examples illustrate that it will be possible to control the dark reversion rate through engineering of the protein environment, but structural understanding of how this can be achieved is lacking.

Here, we solve the protein structures at several time points during dark reversion of the bathy phytochrome from *Pseudomonas aeruginosa*. Intriguingly, we observe strongly asymmetric dark reversion, where only one protomer reverts to form a hybrid PrPfr state. This raises the opportunity for identifying the structural mechanisms with which the thermal isomerization of the biliverdin is controlled.

Results

PrPfr heterodimer is confirmed as dark reversion intermediate

In order to solve the structure of the PrPfr heterodimer state during dark reversion of *Pa*BphP, we made use of its expected relative concentration as derived from spectroscopic observation (**Fig. 1a**),[39] and cryo-trapped the protein on electron microscopy grids at 120 s, 300 s and 960 s after photoexcitation with a laser diode at 780nm. At 120 s, a new structural state (**Fig. 1b, c**) emerges in the protein ensemble (approximately 58% of the particles) along the known PrPr structure (see **Fig. S2** for details of the reconstruction).[26] At 300 s, the new state dominates the ensemble on the grids. Neither the homodimeric PrPr nor the PfrPfr states could be separately reconstructed, but a small number of open, PfrPfr-like particles can be identified during 2D classification (**Fig. S3**). At 960 s, a mixture of the new state (approximately 64% of all particles) and the open PfrPfr state (approximately 34%) is present (**Fig. S4**).

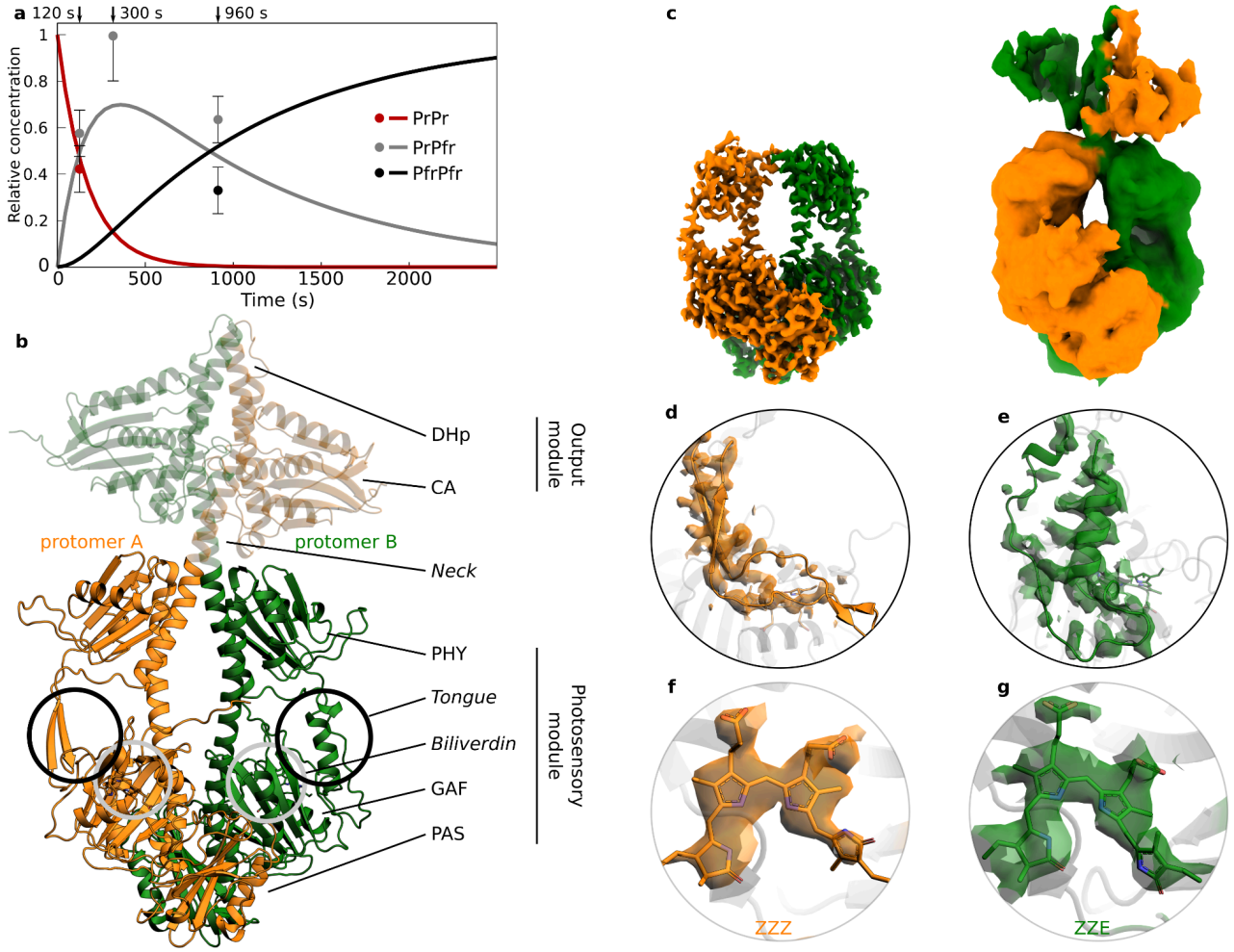

Fig. 1. The dark reversion intermediate of* Pa*BphP is a PrPfr hybrid. *(a) The emergence of the intermediate state was revealed by UV-Vis absorbance spectroscopy at 20°C.[39] The time points at which cryo-EM data were recorded are indicated. The dots show the relative concentrations estimated from the number of particles assigned to each 3D volume in the reconstructions; the error bars are set to 0.1. The error bar for the PrPfr state at the 300s time point is 0.2, to reflect that PfrPfr particles were observed as 2D classes, and that PrPr particles are likely included in the 3D volume for the hybrid state, but that neither of the homodimer states could be refined. (b) The cryo-EM structure of the PrPfr hybrid, reconstructed from the 300 s dark reversion data (the output module, not clearly resolved in the reconstruction, is not included in the final model but is shown here with decreased opacity). (c) The insets show the coulomb density reconstructed via heterogeneous reconstruction of the full-length protein (right) and local refinement of the PSM (left). (d-g) The key*

structural features related to the photocycle: the PHY-tongue (d, e) and the chromophore (f, g) agree with the separate assignments for the protomers.

The newly observed structural state is a PrPfr heterodimer (**Fig. 1b**) with one protomer in Pr and the other one in Pfr, as judged based on the secondary structure of the PHY-tongue (**Fig. 1d, e**), isomerization state and location of the chromophore (**Fig. 1f, g**), and the rotamerization states of key residues lining the binding pocket (**Fig. S5**). The structure of the PrPfr heterodimer was highly similar at all three time points and was, next to the already known PrPr and PfrPfr states, the only structural state identified from the particle ensemble at any of the time points.[26] It is difficult to determine the fractional population of the three states quantitatively from the analysis of the cryo-EM data, however, the estimated concentrations agree well with the kinetic prediction (**Fig. 1a**). This confirms that the spectroscopic intermediate indeed is a PrPfr heterodimer.

Two geometries at the dimer interface resolved for PrPfr and PrPr states

The observed PrPfr heterodimer structure is naturally asymmetric at the tongue and chromophore regions, due to the different photochromic states. However, we also observe strong asymmetry beyond these regions at the dimer interface of the PAS/GAF domains. Here, two distinct geometries are observed. In geometry I, consisting of the GAF_A and PAS_B domains (subscripts denoting the protomer), helix A_A is in a conformation consistent with the Pfr state crystal structure, making contact with $spine_B$, but not connecting to PAS_B. This results in an open interface (**Fig. 2b and d**).[17] Geometry II involves GAF_B and PAS_A and here $helixA_B$ is oriented into a 3-helix bundle with helix B_B, $spine_B$, and makes direct contact with PAS_A - resulting in a closed interface (**Fig. 2b and e**). Highly similar geometries are also observed for the PrPr state (**Fig. 2a**).[26] **Fig. 2c-e** visualize how the interaction network of helix A changes between the two interface geometries. Several key interactions change, affecting the neighbouring spine helix, helix B, and the connection to residues in the PAS domain. We conclude that the interface region at the PAS-GAF domains is intrinsically asymmetric in PrPr and PrPfr (but not in PfrPfr)[26] and that the positioning of helix A plays a decisive role in breaking the symmetry. During reconstruction of the cryo-EM maps, this asymmetric dimer arrangement drives alignment, resulting in high-confidence assignments for protomers A and B in both the PrPr and PrPfr states.

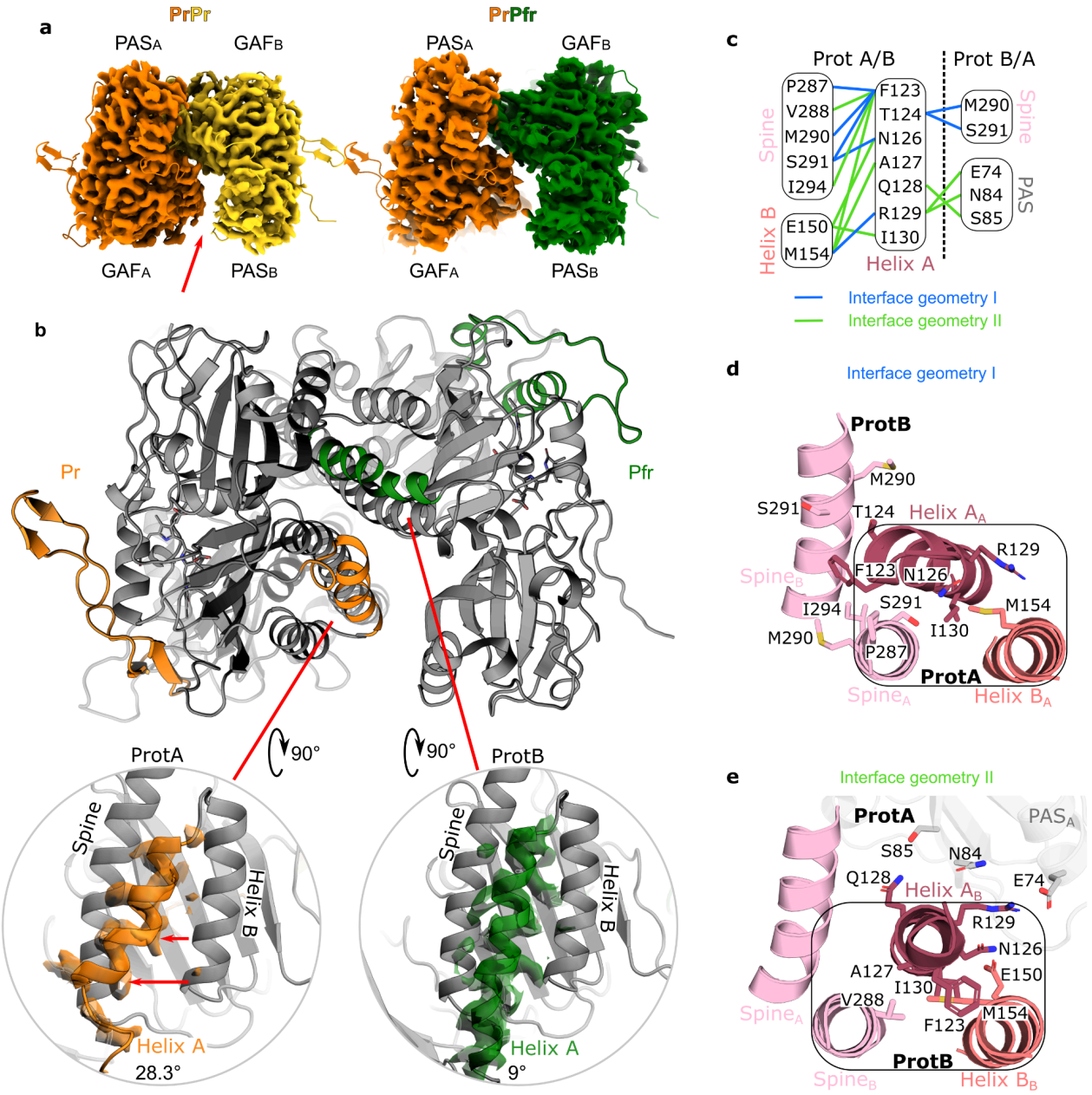

Fig. 2. The PSM dimer interface is asymmetric in both the PrPr ground state and the PrPfr intermediate. *(a) Two distinct PAS-GAF interaction geometries are observed in the PrPr and the hybrid PrPfr states, conserved during the transition from one to the other (red arrow points at the gap related to geometry I). (b) The orientation of helix A differs between the two protomers and correlates strongly with the photochromic state of the protomer in PrPfr: the relaxed helix A, the α-helical PHY tongue and ZZE state chromophore are all exclusive to protomer B (green). This implies a strongly asymmetric dark reversion reaction, in which only protomer B dark converts from PrPr to PrPfr. The angle in the insets is calculated between helix A (residues 123-136) and the base of the spine helix (residues 286-300). (c) Distinct interface geometries according to interactions (interaction frequency differences) for each Helix A of PrPr are shown schematically. Geometry I (blue) shows interactions of ProtB and geometry II (green) shows interactions of ProtA. Structural representations highlight the shift from interactions of Helix A_A to $Spine_B$ (d) to interactions of Helix A_B with PAS_A (e).*

Only one protomer of the asymmetric dimer dark-reverts from PrPr to the PrPfr hybrid state.
Since the asymmetric arrangement of the PAS/GAF dimer interface is retained between PrPr and PrPfr, it provides a handle to trace protomers A and B separately in their dark reversion process. If the dark reversion was stochastic between the protomers, either protomer A or B could backconvert, and blurred densities would be expected at the chromophore and tongue positions because the two conformations would be averaged over each other. However, this is not observed. Instead, we recover high-resolution information at the chromophore and tongue in both protomers, which allows clear assignment to each one of the photochromic states (**Fig. 1 d-g**). This leads to the surprising conclusion that only one of the protomers (protomer B) is observed to dark-revert from the PrPr to the hybrid PrPfr state. The dark reversion reaction in protomer A must be very slow or inhibited. It seems very likely that the difference in reactivity is caused by the observed structural asymmetry of the dimer in PrPr.

A switch of H277 and its hydrogen bonding to the chromophore explains how dark reversion is controlled.
Control over dark reversion requires regulation of the isomerization reaction at the biliverdin. In order to identify this mechanism, we reanalyzed our previously published electron density map (EMD-19981) and model (PDB 9EUT) of the PrPr state.[26] **Fig. 3a** and **c** show that the density around the biliverdin in protomer B is weaker than in protomer A, which indicates a higher degree of heterogeneity in protomer B compared to A. Moreover, there is a difference in the conformation of the conserved histidine 277 (H277) with respect to the biliverdin: in protomer A the distance of the carbonyl oxygen of ring D of the BV (OD) to the epsilon nitrogen on the histidine (NE) is 2.6 Å with an angle of 150°, which is a suitable hydrogen bonding geometry; while in protomer B this distance is increased to 2.9 Å with an angle of 110°, which is not well compatible with hydrogen bonding in protomer B. Local resolution of the maps around the chromophore is ~2.4 Å, which allows for confident placement of the histidine side chains.[26] Additionally, the maps provide clear support for the refined positions of His277 as its electron density extends further towards the BV in protomer A compared to B **(Fig. 3a** and **c**). These structural observations indicate that when hydrogen bonding of H277 to the D-ring carbonyl is direct as in protomer A, the dark reversion reaction becomes inhibited.

To further elucidate the dynamics of the biliverdin and H277, we performed three repetitions of molecular dynamics simulations (MD) for both the PrPr and PrPfr states. Within the 250 ns simulation time, the interface geometries predominantly stayed constant (**Fig. S6**). Using these trajectories, we performed an interaction analysis, where the frequency of contacts between residues is determined according to geometric and electrostatic cutoffs. Higher interaction frequencies thereby indicate a higher stability of the state. We find two predominant conformations, where H277 either forms a hydrogen-bond directly to the D-ring (pattern "H-OD", **Fig. 3d** and **S1**) or it forms a bond via a water molecule to the propionate group of ring C (pattern "H-H2O", **Fig. 3f**). The switch is manifested by retracting and twisting movement of the imidazole ring of H277 which leads to the change of hydrogen bonding. The fact that the trajectories sample both conformations in all of our relatively short MD trajectories implies that the states are close in energy and that they can interconvert within nanoseconds (**Fig. S8**). The switch in hydrogen bonding of H277 has a direct effect on the conformation of the D-ring, which twists around V5 (torsion between C and D ring, NC-C14-C15-C16, see numbering in **S1**) by 7.1° (**Fig. S7**).

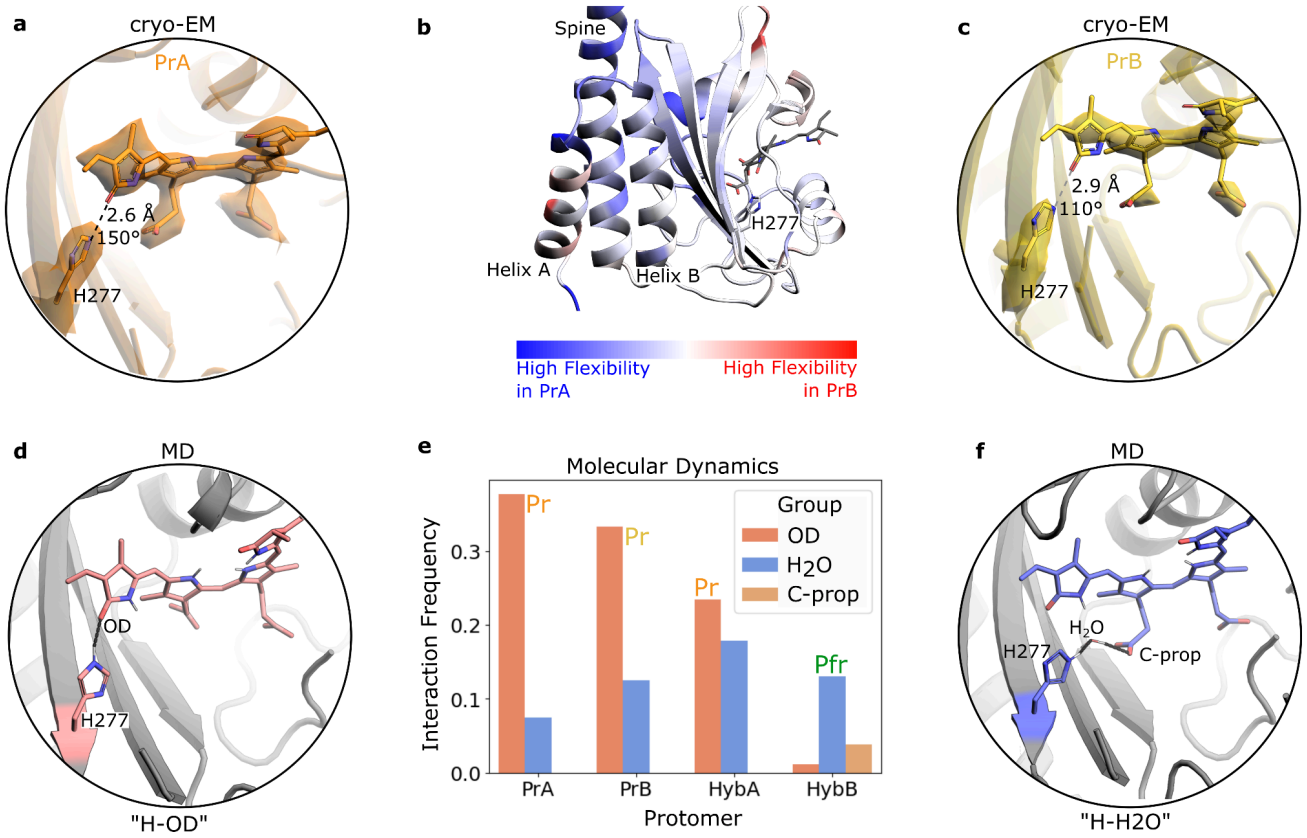

Fig. 3. Distinct interaction pattern of H277 with BV reveals back-reversion advantage of protomer B. *(a, c) Densities of biliverdin at identical contour levels in protomers of PrPr with distances from H277-NE to BV-OD and angles from H277-NE via H277-H_{NE} to BV-OD. (b) The difference in RMSF of the two protomers (which is comparable to an experimental B-factor and a measure for residue-wise flexibility) and highlights a rigidification in protomer B around the active site. (e) Polar contact (hydrogen bonds) frequency of the different protomers where H277 interacts with biliverdin (H277-OD, "H-OD") directly or via bridging waters (H277-H2O-Cprop, "H-H2O") in each protomer of PrPr (PrA and PrB) and PrPfr (HybA and HybB). (d, f) Structural evaluation of the different states of the binding pocket: (d) H277-OD and (f) H277-H2O-Cprop. OD is the carbonyl of the D-ring and C-prop describes the carboxylates of the C-propionate.*

Fig. 3e summarizes the frequencies with which each of the two predominant conformations occurs in the simulations. For the PrPr state, we find that the "H-OD" pattern is prevalent in protomer A ("H-OD" ~38 %, "H-H2O" ~7 %). In protomer B, the occurrence of the "H-H2O" increases while "H-OD" decreases ("H-OD" ~33 %, "H-H2O" ~12 %). This suggests that hydrogen bonding between H277 and the D-ring is tighter in the non-reactive protomer A. While the absolute frequencies of these patterns from MD trajectories may not be 100% reliable because of computational limitations (i.e. imperfect force field and water model), the increased "H–H2O" interactions observed between the two otherwise highly similar protomers support the robustness of the observed trend. Importantly, the structural features align with observations from cryo-EM maps (**Fig. 3a** and **c**). The observation suggests that the regulation of the dark reversion reaction occurs by control of the abundance of the reversion-ready "H-H2O" conformation, where H277 is not bound to the D-ring.

Turning to the MD simulations of the hybrid PrPfr state, we intriguingly find that the "H-H2O" conformation of H277 in protomer A increases in frequency compared to PrPr ("H-OD" ~23 %, "H-H2O" ~18 %). This finding is supported by the cryo EM structures of the hybrid state, where the H277 in protomer A of PrPfr is refined into a position with distance of 2.6 Å and 120° with respect to

the D-ring carbonyl, which is a conformation that resembles that of protomer B in PrPr and is unfavourable for direct hydrogen bonding. This suggests that protomer A can now undergo dark reversion from PrPfr to PfrPfr (**Fig. 3e**).

Protein dynamics link the H277 switch to conformation of the dimer interface.
Having established the importance of the positioning of H277 for dark reversion (**Fig. 3**) it is interesting to find out how the asymmetry at the dimer interface and in particular the positioning of helix A (**Fig. 2**) are connected to this molecular switch. Inspection of the MD trajectories and the cryo-EM structures did not reveal a clear pathway of concerted structural changes. Instead, we find correlated differences in the dynamics as modelled by the MD simulations. In helix B of protomer A, the spine helix, and the five-membered beta-sheet of the PAS domain, which connects to H277, are notably more flexible than in protomer B according to the RMSF (**Fig. 3b**). Only helix A is more rigid in protomer A pointing at a stabilization due to the formed interactions with $spine_B$. The observation suggests that the asymmetric arrangement of helix A at the interface (geometry I, **Fig. 2d**) and the reactivity of the biliverdin are connected via altered dynamics of the PAS/GAF domains. Rigidification of the active site enables stabilization of the surrounding residues and thus opens up the space for rearrangements in H277 and the BV itself.

The H277 switch and interface conformations explain allostery in the dark reversion reaction.
From the structures and supported by the MD simulations, we find two patterns of hydrogen bonding of H277, which correlate with the dark reversion propensities of the two protomers. This leads to strongly asymmetric dark reversion: Thermal isomerization of the biliverdin in protomer A is blocked or prohibitively slow in PrPr, which corresponds to the dominant occurrence of hydrogen bonding of H277 directly to the D-ring. However, in protomer B, the biliverdin is not hydrogen bonded to H277 and the reversion reaction occurs. In the PrPfr heterodimer state, the hydrogen bond pattern of protomer A is altered, with H277 binding much more frequently in the “H-H2O” arrangement, thus freeing up the biliverdin for thermal isomerization. The cryo EM structures show that this molecular switch of H277 is correlated with the asymmetric structure at the dimer interface and the MD simulations suggest that the signal is transduced by modulation of the internal dynamics in the PAS-GAF domains.

Discussion

PrPfr intermediates in the phytochrome photocycle have been described in plants and, more recently, in bacterial systems.[5,20,25,37,38] In plants, it is well established that the intermediates are functionally relevant, enhancing the signalling potential of the protein.[38] Here, we demonstrate that the PrPfr state is a key intermediate in the dark reversion pathway of bacterial phytochromes, structurally confirming our recent spectroscopic assignment.[39] The fact that the hybrid state is allosterically and even asymmetrically regulated suggests that it is not a fleeting intermediate, but that it actively contributes to phytochrome signaling, even in bacteria.

The strong asymmetry in the dark reversion of the two protomers is surprising (**Fig. 4a**). It may be that the phytochromes's function requires asymmetry of the PrPfr state for signalling, however, another interpretation is that the asymmetry is the mechanism with which the rate constants of dark reversion are allosterically controlled. While the observed structural differences of H277 and around the chromophore are rather small, their effects on the dark reversion rates are dramatic. Hence, the protein can make use of the large effect that small changes in activation energy can have on kinetic rates. We propose that phytochromes control the abundance of the states that have fast vs slow recombination dynamics.

Signalling in phytochromes involves a number of structural elements, including the chromophore and its direct environment, the PHY-tongue, and the output domains.[15–20] In particular, the output domains and linker region have been shown to play a role in the regulation of dark reversion, but a structural explanation for this has been lacking.[18,20,45] Our work highlights the dimer interface geometry of the PAS-GAF domains as a key player in the reaction: helix A is oriented in distinct conformations in the two protomers, which strongly correlates with the ability of the connected chromophore to undergo dark isomerization. It is likely that changes in the output domains are transduced to the chromophore via this route, providing a structural rationale on how the output domains can influence the reactivity of phytochromes over distances of several tens of Ångströms.

Notably, the structural importance of the interface region and helix A in particular is not unique to *Pa*BphP. In the case of the canonical bacteriophytochrome *Sa*BphP2, for which the PrPr, PrPfr, and PfrPfr states also have been solved, the same helix adopts different conformations in the photochromic states (**Fig. S9**).[25] While there is no inherent asymmetry in its dark or photoactivated states, the PrPfr heterodimer presents an asymmetric dimer interface. It is conceivable that this allosterically controls the rate constants of reversion even for *Sa*BphP2.

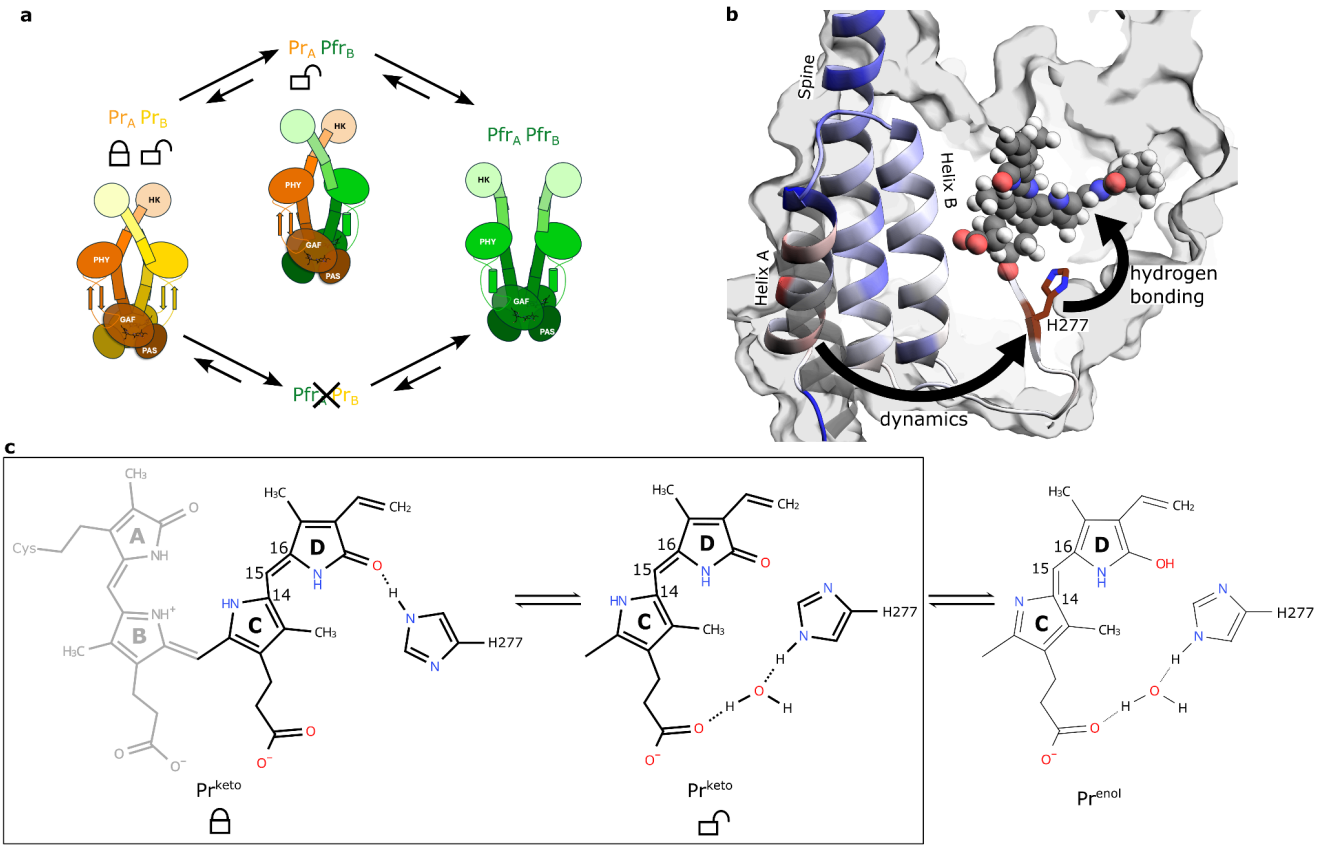

Fig. 4. Summary of the asymmetric dark reversion mechanism. *(a) Schematic asymmetric dark reversion shows that only one of the pathways is available and unlocks protomer A in the hybrid state for complete dark reversion to PfrPfr. Open and closed locks symbolize the dark reversion accessible or inaccessible protomers. (b) Close-up of a phytochrome PAS-GAF domain shows the influence of the asymmetric interface (Helix A) on H277 (dynamics) and BV (hydrogen bonding). The helices are colored according to the difference in RMSF of the two protomers (blue means protomer A is more flexible) and the alternative conformation of helix A is shown in grey. (c) Combining the keto-enol tautomerization idea by Escobar et. al.[43] with the difference in hydrogen bonding of H277 described in this work (in the black box).*

Our data reveal that the conserved H277 and the surrounding hydrogen-bonding network play a key role in regulating the dark reversion reaction. H277 is widely, but not universally, conserved across the phytochrome family. In agreement with the theory that the hydrogen bonding environment of the D-ring controls the isomerization yield in the photoreaction,[46,47] mutational alteration of H277 changes the time scale and yield of the forward photoreaction, but it does not inhibit it.[29,48] Here, we find that its positioning is responsible for regulation of the dark reversion. In the PrPr state, H277 adopts two distinct conformations: one forms a direct hydrogen bond with the D-ring carbonyl (dominant in protomer A), while the other connects via a water bridge to the C-propionate, effectively removing the interaction with the D-ring (**Fig. 4c**). The direct hydrogen bond blocks dark reversion, whereas the water-mediated configuration enables the D-ring to rotate, facilitating ZZZ-to-ZZE isomerization.

It has been shown that the dark reversion in bathy phytochromes proceeds via a keto–enol tautomerization mechanism.[43] Here, internal proton transfer from the B/C-rings to the D-ring carbonyl reduces the double-bond character between C15 and C16, thereby lowering the activation energy for ring rotation. The here-discovered switch by H277 is in agreement with this and provides a mechanistic explanation: when H277 binds to the D-ring carbonyl, it stabilizes the keto form and inhibits tautomerization into the enol form (**Fig. 4c, left**). In this arrangement, the BV cannot undergo

isomerization, because the activation energy is too high. When H277 switches to its alternative conformation, the carbonyl is freed from hydrogen bonding, may transition into the enol form, and dark reversion can proceed. The pH dependence of the dark reversion rates in the bathy phytochrome from *Agrobacterium fabrum* indicated the involvement of a histidine,[43] which we confirm here structurally. Since the enol form is expected to have a very much lower activation energy compared to the keto form, this readily explains why small changes in H277 positioning have large effects on the rate of dark reversion.

Structural heterogeneity has been inferred for phytochromes from NMR and time-resolved optical spectroscopy experiments.[21,49–51] Here, we detect the structural heterogeneity directly in the PrPr and hybrid PrPfr states, which is connected to asymmetry across the dimer. The distribution of the two H277 arrangements is not equal, because the coupling between the asymmetric dimer arrangements and the chromophore, which happens through changes in protein dynamics, is rather weak (**Fig. 4b**). We propose that control over the rigidity of the PAS-GAF domains provides the evolution of a versatile handle to optimize dark reversion rates of phytochromes. An interesting idea would be that the unique knot present in all phytochromes may provide the stability in the PAS/GAF domains needed for fine-tuning of the dynamics that transmit the signal from the asymmetric binding of helix A at the dimer interface to H277.

Our structural observation of the PrPfr hybrid state as a key intermediate of dark reversion provides a chemical mechanism on how phytochromes control isomerization rates. Allosteric control of these rates is a common feature of phytochromes, and here we identify two interface arrangements and a switch in hydrogen bonding by H277 as underlying chemical factors.[37,52] The mechanism identifies a new communication channel between the two protomers of the phytochrome homodimer via protein dynamics. We hope that the chemical understanding of the isomerization reaction is of use for the design of novel optogenetic phytochrome variants.

Methods

Protein purification

*Pa*BphP was recombinantly expressed in *E. coli* BL21 cells transformed with the *Pa*BphP gene (GenBank: AAG07504.1, on a pET28a(+) backbone) and a heme oxygenase gene was kindly provided by Prof. Janne A. Ihalainen. The cells were grown in LB media containing 50 µg/mL kanamycin and 34.5 µg/mL chloramphenicol at 37°C until OD_{600} reached 0.6, then supplemented with 1 mM IPTG and 1 mM 5-aminolevulinic acid before lowering the incubation temperature to 18°C.

The cells were processed in lysis buffer (50 mM Tris, 150 mM NaCl, 10% glycerol, 10 U/mL of DNase 1 and one tablet of cOmplete EDTA-free protease inhibitor (Roche) at pH 8.0) using an EmulsiFlex C3 homogeniser (Avestin), and the lysate briefly incubated with a molar excess of biliverdin hydrochloride. The protein was then purified through a two-step chromatography protocol: first, Ni-NTA affinity chromatography (HisTrap HP 5 mL, Cytiva) by washing the bound sample with wash buffer (50 mM Tris and 1 M NaCl at pH 8.0) and eluting with elution buffer (50 mM Tris, 50 mM NaCl, 300 mM imidazole at pH 8.0); followed by size-exclusion chromatography (HiLoad 16/600 Superdex 200 pg, Cytiva) in SEC buffer (30 mM Tris at pH 8.0). The purified protein was collected at a concentration of 3 mg/mL and flash-frozen for storage.

Cryo-electron microscopy specimen preparation

For structural studies, the protein was diluted to 1.5 mg/mL and the buffer exchanged to 80 mM Tris, 10 mM MgCl2 and 150 mM CH3CO2K at pH of 7.8. The bulk sample was illuminated with a 780 nm light source over 30 s (total dose: ~1 mJ/mm^2), then left in complete darkness until deposition on glow discharged UltrAuFoil (Quantifoil) R 1.2/1.3 (300 mesh) grids and flash-freezing in liquid ethane. The dark reversion time was measured from the removal of the far-red light source and was considered terminated at the moment of flash freezing. Specimens with 120, 300 and 960 seconds of dark reversion were prepared. The laser dose is sufficient to achieve full conversion into Pr.

Cryo-electron microscopy data collection

The specimens were imaged using a Titan Krios G2 (Thermo Scientific) 300 keV transmission electron microscope equipped with a K3 (Gatan) detector and a BioQuantum (Gatan) energy filter. The data acquisition settings were as follows: 0.828 Å/px (105kx magnification), 50 $e/Å^2$ total electron dose, -0.8 to -2.0 mm defocus range, 20 eV energy filter slit width. Automated collection was performed using the EPU software (Thermo Scientific). A total of 13,534movies were collected for the 120 s time point, 14,573 movies for the 300 s time point, and 13,112 movies for the 960 s time point.

Cryo-electron microscopy data processing

The collected micrographs were processed using Cryosparc v4.6.2. Preprocessing consisted of patch motion correction, patch CTF estimation and micrograph denoising (only for visualization purposes). A total of 13,393, 14,033, and 10,323 high-quality micrographs were accepted based on CTF fit, average defocus and relative ice thickness. Particles were originally picked as 80-180 Å blobs. For the 300 s dataset, a Topaz model was trained for more accurate picking, whereas in the other datasets the originally picked particle sets were used for further refinement. Removal of junk particles was done by subsequent rounds of 2D classification and heterogeneous refinement using both the open and closed dimers and several "junk" volumes as references.

For the 300 s dataset, a total of 964,467 particles were identified, which contributed to a PrPfr reconstruction. Further 3D classification did not reveal a separate PrPr class, but it was used to further select 488,190 particles with especially well-ordered α-helices in the PHY_B region (**Fig. S3**). Separate local refinements were conducted with masks for the PAS-GAF-PHY regions of protomers A and B, which yielded maps of global resolution 2.87 and 2.85 Å, respectively. The output module was resolved at a nominal resolution of 5.4 Å. An atomic model was built using the ISOLDE (v1.6) extension of ChimeraX (v1.8), with the models 9EUY and 9EUT used as templates.[26,53] The two locally refined maps were then combined using the Phenix function 'Combine focused maps'.

For the 120 s dataset, a total of 895,611 particles were found. These were subjected to 3D classification using the "simple" initialization mode to reveal reconstructions of both the PrPr and the PrPfr states, followed by a second, targeted 3D classification round. 376,742 (42.1%) of the particles contributed to the PrPr map, while 513,575 particles (57.9%) yielded a PrPfr volume (Fig. S2). Local refinements of the PAS-GAF-PHY regions (excluding the output module) were conducted on both classes, resulting in global resolutions of 3.02 and 2.82 Å, respectively. Comparing the two maps against 9EUT and the newly built PrPfr models showed good fits, so no new model was built into these refinements.

For the 960 s dataset, a total of 476,372 particles were identified, with 303,375 (63.7%) contributing to a PrPfr map at 3.07 Å resolution, and 172,997 (36.3%) particles belonging to an open PfrPfr reconstruction, resolved at 3.29 Å resolution (**Fig. S4**).

Estimation of relative concentrations at each time point was done by generating a consensus reconstruction (where applicable), then splitting the final particle set into Pr/PrPfr/Pfr groups by 3D classification in input initialization mode, supplying high-resolution (<3 Å) input maps and filtering to 4 Å.

Molecular dynamics simulations

We performed molecular dynamics simulations of both the full length PrPr and hybrid PrPfr states. Thus, the structures were protonated with H++ at pH 8 according to the experimental conditions (H277 is protonated as HIE).[54–57] As force-field ff14SB[58] was used as well as the TIP3P[59] water model (10 Å minimum wall distance),[60,61] utilizing the AMBER24 tool kit, i.e. the tleap implementation.[62] Charges were neutralized with a uniformal background charge and the systems were equilibrated with a multi-step protocol. [58,63,64]

Both systems were simulated for approximately 250 ns three times (see **Table 1**) in an NpT ensemble (using pmemd.cuda),[65] using a timestep of 2 fs, since the SHAKE algorithm was applied.[65,66] The particle-mesh Ewald (PME) method took care of electrostatic interactions. The langevin thermostat kept the temperature at 300 K and the monte carlo barostat kept pressure at 1 bar. [67,68]

The performed simulations were analysed and visualised with cpptraj, vmd and pymol. RMSF (Root mean square fluctuation) calculations and interaction analysis were performed with cpptraj and the GetContacts tool and an associated python script.[69–71] (https://getcontacts.github.io/, [72] For the RMSF the structures were aligned on the respective GAF domain before calculation of the RMSF which were thus subtracted from one another (scale ranges between 2 Å). To show that the assignment is reliable we calculated the difference of each protomer A to each protomer B across all PrPr simulations (**Fig.**

S10). For the hydrogen bond analysis of H277 we used the cpptraj command hbond and selected as donor H277 and as acceptor the chromophore. For the interface interaction analysis, we combined hydrogen bonds, salt bridges and van der Waals interactions calculated with GetContacts and applied a cutoff of 0.5 for the difference between the interaction frequencies to highlight the main differences between the two geometries.

Table 1. *Summary of simulation frames and time of all repetitions.*

Simulation repetitions	**PrPr**		**PrPfr**	
	Frames	**Time**	**Frames**	**Time**
1	12465	249 ns	11901	238 ns
2	17832	357 ns	12500	250 ns
3	16472	329 ns	15271	305 ns

Acknowledgements

We acknowledge the use of the Cryo-EM Uppsala facility for cryo-EM specimen preparation and screening, funded by the Department of Cell and Molecular Biology, the Disciplinary Domains of Science and Technology and of Medicine and Pharmacy at Uppsala University.

The cryo-EM data was collected at the Cryo-EM Swedish National Facility funded by the Knut and Alice Wallenberg, Family Erling Persson and Kempe Foundations, SciLifeLab, Stockholm University and Umeå University.

The molecular dynamics computations were partially enabled by resources provided by the National Academic Infrastructure for Supercomputing in Sweden (NAISS), i.e. the PDC Center for High Performance Computing at KTH Royal Institute of Technology, partially funded by the Swedish Research Council through grant agreement no. 2022-06725.

S.W. acknowledges funding from the Swedish Research Council (grant no. 2021-05101).

Supplementary information

Supplementary file 1 containing Supplementary Fig.s 1-10

Data availability

The composite cryo-EM map used to reconstruct the PrPfr model has been deposited in EMDB (EMD-53916). The PrPfr model has been deposited in the Protein Data Bank (9RCC). Raw movies and final particle sets for the time points have been deposited in EMPIAR (EMPIAR-12874). Molecular dynamics simulations have been deposited in Zenodo (10.5281/zenodo.15796800).

References

1. Butler, W. L., Norris, K. H., Siegelman, H. W. & Hendricks, S. B. DETECTION, ASSAY, AND PRELIMINARY PURIFICATION OF THE PIGMENT CONTROLLING PHOTORESPONSIVE DEVELOPMENT OF PLANTS. *Proc Natl Acad Sci U S A* **45**, 1703–1708 (1959).
2. Hughes, J. *et al.* A prokaryotic phytochrome. *Nature* **386**, 663 (1997).
3. Davis, S. J., Vener, A. V. & Vierstra, R. D. Bacteriophytochromes: phytochrome-like photoreceptors from nonphotosynthetic eubacteria. *Science* **286**, 2517–2520 (1999).
4. Hughes, J. & Winkler, A. New Insight Into Phytochromes: Connecting Structure to Function. *Annu Rev Plant Biol* **75**, 153–183 (2024).
5. Schäfer, E. & Schmidt, W. Temperature dependence of phytochrome dark reactions. *Planta* **116**, 257–266 (1974).
6. Jung, J.-H. *et al.* Phytochromes function as thermosensors in Arabidopsis. *Science* **354**, 886–889 (2016).
7. Casal, J. J. Photoreceptor signaling networks in plant responses to shade. *Annu. Rev. Plant Biol.* **64**, 403–427 (2013).
8. Franklin, K. A. & Quail, P. H. Phytochrome functions in Arabidopsis development. *J. Exp. Bot.* **61**, 11–24 (2010).
9. Legris, M., Ince, Y. Ç. & Fankhauser, C. Molecular mechanisms underlying phytochrome-controlled morphogenesis in plants. *Nat. Commun.* **10**, 5219 (2019).
10. Hughes, J. Phytochrome cytoplasmic signaling. *Annu Rev Plant Biol* **64**, 377–402 (2013).
11. Njimona, I., Yang, R. & Lamparter, T. Temperature effects on bacterial phytochrome. *PLoS One* **9**, e109794 (2014).
12. Burgie, E. S. & Vierstra, R. Phytochromes: An Atomic Perspective on Photoactivation and Signaling. *Plant Cell* **26**, 4568–4583 (2014).
13. Vierstra, R. D. & Davis, S. J. Bacteriophytochromes: new tools for understanding phytochrome signal transduction. *Semin Cell Dev Biol* **11**, 511–521 (2000).
14. Takala, H., Edlund, P., Ihalainen, J. A. & Westenhoff, S. Tips and turns of bacteriophytochrome photoactivation. *Photochem Photobiol Sci* **19**, 1488–1510 (2020).
15. Takala, H. *et al.* Signal amplification and transduction in phytochrome photosensors. *Nature* **509**, 245–248 (2014).
16. Essen, L.-O., Mailliet, J. & Hughes, J. The structure of a complete phytochrome sensory module in the Pr ground state. *Proc Natl Acad Sci U S A* **105**, 14709–14714 (2008).
17. Yang, X., Kuk, J. & Moffat, K. Crystal structure of Pseudomonas aeruginosa bacteriophytochrome: photoconversion and signal transduction. *Proc Natl Acad Sci U S A* **105**, 14715–14720 (2008).
18. Gourinchas, G. *et al.* Long-range allosteric signaling in red light-regulated diguanylyl cyclases. *Sci Adv* **3**, e1602498 (2017).
19. Björling, A. *et al.* Structural photoactivation of a full-length bacterial phytochrome. *Science Advances* (2016)

doi:10.1126/sciadv.1600920.

20. Gourinchas, G., Heintz, U. & Winkler, A. Asymmetric activation mechanism of a homodimeric red light-regulated photoreceptor. *Elife* **7**, (2018).
21. Song, C. *et al.* Two ground state isoforms and a chromophore D-ring photoflip triggering extensive intramolecular changes in a canonical phytochrome. *Proc Natl Acad Sci U S A* **108**, 3842–3847 (2011).
22. Li, H., Burgie, E. S., Gannam, Z. T. K., Li, H. & Vierstra, R. D. Plant phytochrome B is an asymmetric dimer with unique signalling potential. *Nature* **604**, 127–133 (2022).
23. Burgie, E. S. *et al.* The structure of Arabidopsis phytochrome A reveals topological and functional diversification among the plant photoreceptor isoforms. *Nat. Plants* **9**, 1116–1129 (2023).
24. Wahlgren, W. Y. *et al.* Structural mechanism of signal transduction in a phytochrome histidine kinase. *Nat Commun* **13**, 7673 (2022).
25. Malla, T. N. *et al.* Photoreception and signaling in bacterial phytochrome revealed by single-particle cryo-EM. *Sci Adv* **10**, eadq0653 (2024).
26. Bódizs, S., Mészáros, P., Grunewald, L., Takala, H. & Westenhoff, S. Cryo-EM structures of a bathy phytochrome histidine kinase reveal a unique light-dependent activation mechanism. *Structure* **32**, 1952–1962.e3 (2024).
27. Wang, Z. *et al.* Light-induced remodeling of phytochrome B enables signal transduction by phytochrome-interacting factor. *Cell* **187**, 6235–6250.e19 (2024).
28. Nagano, S. *et al.* Pr and Pfr structures of plant phytochrome A. *Nature Communications* **16**, 1–12 (2025).
29. Björling, A. *et al.* Ubiquitous Structural Signaling in Bacterial Phytochromes. *J Phys Chem Lett* **6**, 3379–3383 (2015).
30. Medzihradszky, M. *et al.* Phosphorylation of phytochrome B inhibits light-induced signaling via accelerated dark reversion in Arabidopsis. *Plant Cell* **25**, 535–544 (2013).
31. Frankland, B. Biosynthesis and dark transformations of phytochrome. (1972) doi:10.5555/19730709563.
32. Anderson, G. R., Jenner, E. L. & Mumford, F. E. Temperature and pH studies on phytochrome in vitro. *Biochemistry* **8**, 1182–1187 (1969).
33. Sweere, U. *et al.* Interaction of the response regulator ARR4 with phytochrome B in modulating red light signaling. *Science* **294**, 1108–1111 (2001).
34. Eichenberg, K. *et al.* Arabidopsis phytochromes C and E have different spectral characteristics from those of phytochromes A and B. *FEBS Lett* **470**, 107–112 (2000).
35. Yi, C. *et al.* Plant Phytochrome Interactions Decode Light and Temperature Signals. *Plant Cell* **36**, 4819–4839 (2024).
36. Legris, M. *et al.* Phytochrome B integrates light and temperature signals in Arabidopsis. *Science* **354**, 897–900 (2016).
37. Hennig, L. & Schäfer, E. Both subunits of the dimeric plant photoreceptor phytochrome require chromophore for

stability of the far-red light-absorbing form. *J Biol Chem* **276**, 7913–7918 (2001).

38. Klose, C. *et al.* Systematic analysis of how phytochrome B dimerization determines its specificity. *Nat Plants* **1**, 15090 (2015).
39. Prodhan, S. *et al.* Detection of a hybrid PrPfr state in the dark reversion of a bathy phytochrome indicates inter-dimer allostery. *bioRxiv* 2025.05.28.656462 (2025) doi:10.1101/2025.05.28.656462.
40. Altoè, P. *et al.* Deciphering intrinsic deactivation/isomerization routes in a phytochrome chromophore model. *J. Phys. Chem. B* **113**, 15067–15073 (2009).
41. Lagarias, J. C. & Rapoport, H. Chromopeptides from phytochrome. The structure and linkage of the PR form of the phytochrome chromophore. *J. Am. Chem. Soc.* **102**, 4821–4828 (1980).
42. Villegas-Escobar, N. & Matute, R. A. The Keto-Enol Tautomerism of Biliverdin in Bacteriophytochrome: Could it Explain the Bathochromic Shift in the Pfr Form? *Photochem Photobiol* **97**, 99–109 (2021).
43. Velazquez Escobar, F. *et al.* A protonation-coupled feedback mechanism controls the signalling process in bathy phytochromes. *Nat Chem* **7**, 423–430 (2015).
44. Wang, D. *et al.* The Origin of Ultrafast Multiphasic Dynamics in Photoisomerization of Bacteriophytochrome. *J Phys Chem Lett* **11**, 5913–5919 (2020).
45. Takala, H., Björling, A., Linna, M., Westenhoff, S. & Ihalainen, J. A. Light-induced Changes in the Dimerization Interface of Bacteriophytochromes. *J Biol Chem* **290**, 16383–16392 (2015).
46. Chenchiliyan, M. *et al.* Ground-state heterogeneity and vibrational energy redistribution in bacterial phytochrome observed with femtosecond 2D IR spectroscopy. *J Chem Phys* **158**, 085103 (2023).
47. Salvadori, G. & Mennucci, B. Analogies and Differences in the Photoactivation Mechanism of Bathy and Canonical Bacteriophytochromes Revealed by Multiscale Modeling. *J Phys Chem Lett* **15**, 8078–8084 (2024).
48. Mathes, T. *et al.* Femto- to Microsecond Photodynamics of an Unusual Bacteriophytochrome. *J Phys Chem Lett* **6**, 239–243 (2015).
49. Kim, P. W., Rockwell, N. C., Martin, S. S., Clark Lagarias, J. & Larsen, D. S. Heterogeneous Photodynamics of the Pfr State in the Cyanobacterial Phytochrome Cph1. (2014) doi:10.1021/bi5005359.
50. Yang, Y. *et al.* Active and silent chromophore isoforms for phytochrome Pr photoisomerization: An alternative evolutionary strategy to optimize photoreaction quantum yields. *Struct Dyn* **1**, 014701 (2014).
51. Lim, S. *et al.* Correlating structural and photochemical heterogeneity in cyanobacteriochrome NpR6012g4. *Proc Natl Acad Sci U S A* **115**, 4387–4392 (2018).
52. Klose, C., Nagy, F. & Schäfer, E. Thermal reversion of plant phytochromes. *Mol. Plant* **13**, 386–397 (2020).
53. Croll, T. I. ISOLDE: a physically realistic environment for model building into low-resolution electron-density maps.

Acta Crystallogr D Struct Biol **74**, 519–530 (2018).

54. Anandakrishnan, R., Aguilar, B. & Onufriev, A. V. H++ 3.0: automating pK prediction and the preparation of biomolecular structures for atomistic molecular modeling and simulations. *Nucleic Acids Res* **40**, W537–41 (2012).
55. Gordon, J. C. *et al.* H++: a server for estimating pKas and adding missing hydrogens to macromolecules. *Nucleic Acids Res* **33**, W368–71 (2005).
56. Myers, J., Grothaus, G., Narayanan, S. & Onufriev, A. A simple clustering algorithm can be accurate enough for use in calculations of pKs in macromolecules. *Proteins* **63**, 928–938 (2006).
57. H++ (web-based computational prediction of protonation states and pK of ionizable groups in macromolecules). http://newbiophysics.cs.vt.edu/H++/.
58. Maier, J. A. *et al.* ff14SB: Improving the Accuracy of Protein Side Chain and Backbone Parameters from ff99SB. *J Chem Theory Comput* **11**, 3696–3713 (2015).
59. Jorgensen, W. L., Chandrasekhar, J., Madura, J. D., Impey, R. W. & Klein, M. L. Comparison of simple potential functions for simulating liquid water. *J. Chem. Phys.* **79**, 926–935 (1983).
60. El Hage, K., Hédin, F., Gupta, P. K., Meuwly, M. & Karplus, M. Valid molecular dynamics simulations of human hemoglobin require a surprisingly large box size. *Elife* **7**, (2018).
61. Gapsys, V. & de Groot, B. L. Comment on 'Valid molecular dynamics simulations of human hemoglobin require a surprisingly large box size'. *Elife* **8**, (2019).
62. Case, D. A. *et al.* AmberTools. *Journal of Chemical Information and Modeling* (2023) doi:10.1021/acs.jcim.3c01153.
63. Hub, J. S., de Groot, B. L., Grubmüller, H. & Groenhof, G. Quantifying Artifacts in Ewald Simulations of Inhomogeneous Systems with a Net Charge. *J Chem Theory Comput* **10**, 381–390 (2014).
64. Wallnoefer, H. G., Handschuh, S., Liedl, K. R. & Fox, T. Stabilizing of a globular protein by a highly complex water network: a molecular dynamics simulation study on factor Xa. *J Phys Chem B* **114**, 7405–7412 (2010).
65. Salomon-Ferrer, R., Götz, A. W., Poole, D., Le Grand, S. & Walker, R. C. Routine Microsecond Molecular Dynamics Simulations with AMBER on GPUs. 2. Explicit Solvent Particle Mesh Ewald. *J Chem Theory Comput* **9**, 3878–3888 (2013).
66. Miyamoto, S. & Kollman, P. A. Settle: An analytical version of the SHAKE and RATTLE algorithm for rigid water models. *J. Comput. Chem.* **13**, 952–962 (1992).
67. Adelman, S. A. & Doll, J. D. Generalized Langevin equation approach for atom/solid-surface scattering: General formulation for classical scattering off harmonic solids. *J. Chem. Phys.* **64**, 2375–2388 (1976).
68. Molecular dynamics simulations of water and biomolecules with a Monte Carlo constant pressure algorithm. *Chemical Physics Letters* **384**, 288–294 (2004).

69. Roe, D. R. & Cheatham, T. E., 3rd. PTRAJ and CPPTRAJ: Software for Processing and Analysis of Molecular Dynamics Trajectory Data. *J Chem Theory Comput* **9**, 3084–3095 (2013).

70. VMD: Visual molecular dynamics. *Journal of Molecular Graphics* **14**, 33–38 (1996).

71. Schrödinger, L. The PyMOL molecular graphics system, version 1.8. *(No Title)* (2015).

72. Fernández-Quintero, M. L. *et al.* The influence of antibody humanization on shark variable domain (VNAR) binding site ensembles. *Front Immunol* **13**, 953917 (2022).